Suomi NPP VIIRS prelaunch and on-orbit geometric calibration and characterization

Robert E. Wolfe,[1] Guoqing Lin,[2] Masahiro Nishihama,[3] Krishna P. Tewari,[2] James C. Tilton,[1] and Alice R. Isaacman[2]

[1]   The Visible Infrared Imaging Radiometer Suite (VIIRS) sensor was launched 28 October 2011 on the Suomi National Polar-orbiting Partnership (SNPP) satellite. VIIRS has 22 spectral bands covering the spectrum between 0.412 µm and 12.01 µm, including 16 moderate resolution bands (M-bands) with a nominal spatial resolution of 750 m at nadir, five imaging resolution bands (I-bands) with a nominal spatial resolution of 375 m at nadir, and a day-night band (DNB) with a near-constant nominal 750 m spatial resolution throughout the scan. These bands are located in a visible and near-infrared focal plane assembly (FPA), a shortwave and midwave infrared FPA, and a long-wave infrared FPA. All bands, except the DNB, are coregistered for proper environmental data records retrievals. Observations from VIIRS instrument provide long-term measurements of biogeophysical variables for climate research and polar satellite data stream for the operational community's use in weather forecasting and disaster relief and other applications. Well Earth-located (geolocated) instrument data are important to retrieving accurate biogeophysical variables. This paper describes prelaunch pointing and alignment measurements, and the two sets of on-orbit correction of geolocation errors, the first of which corrected error from 1300 m to within 75 m (20% I-band pixel size) and the second of which fine-tuned scan-angle dependent errors, bringing VIIRS geolocation products to high maturity in one and a half years of the SNPP VIIRS on-orbit operations. Prelaunch calibration and the on-orbit characterization of sensor spatial impulse responses and band-to-band coregistration are also described.

1.   Introduction

[2]   The NASA/NOAA Visible Infrared Imaging Radiometer Suite (VIIRS) sensor was launched 28 October 2011 on the Suomi National Polar-orbiting Partnership (SNPP) satellite in a near-circular, sun-synchronous, near-polar orbit having an 840 km mean altitude, 98.7° inclination, an orbital period of 101.5 min, and a nominal ascending equator local crossing time of 13:30 ±10 min. The instrument inherits many features from the Moderate Resolution Imaging Spectroradiometer (MODIS) onboard NASA Earth Observing System (EOS) Terra and Aqua satellites, the advanced very high resolution radiometer (AVHRR) on NOAA's Polar-orbiting Environ-

mental Satellites, the Sea-viewing Wide Field-of-view Sensor (SeaWiFS) on SeaStar, and the Operational Linescan System (OLS) on the U.S. Department of Defense (DoD) Defense Meteorological Satellite Program (DMSP) satellites [*Cao et al.*, 2013]. The observations from SNPP VIIRS continue the long-term measurements from these heritage instruments in the afternoon orbit. VIIRS is also meant to continue the polar satellite data stream for the operational community's use in weather forecasting and disaster relief and other applications. Copies of this instrument will be on the follow-on NOAA Joint Polar Satellite System (JPSS) in the afternoon orbits. Good geometric performance of these instruments is important to retrieving accurate biogeophysical variables for both the long-term monitoring and operational communities.

[3]   This paper describes VIIRS geometric characteristics and performance. Section 2 gives a general description of the instrument's geometric features. Section 3 summarizes the results of geometric calibration and characterization in the ground testing before launch, which includes the sensor's spatial impulse responses, band-to-band coregistration (BBR), and pointing and alignments. The algorithm for on-orbit pointing and geolocation is briefed in section 4. Section 5 describes geolocation error correction and trending in the first one and half years of on-orbit operations. The on-orbit geometric features other than geolocation are characterized in

---
[1]NASA Goddard Space Flight Center, Greenbelt, Maryland, USA.
[2]Innovim, Greenbelt, Maryland, USA.
[3]Sigma Space Corporation, Lanham, Maryland, USA.

Corresponding author: R. E. Wolfe, NASA Goddard Space Flight Center, Greenbelt Rd., Greenbelt, MD 20771, USA. (Robert.E.Wolfe@nasa.gov)
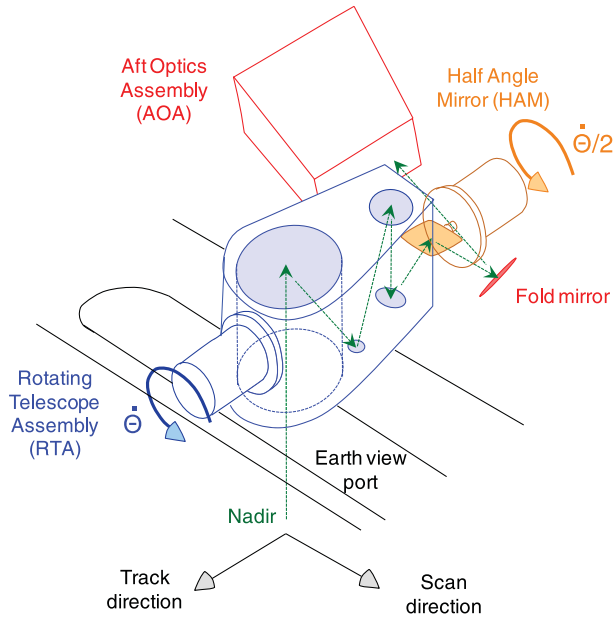
Figure 1. Illustration of the VIIRS scanning system.

section 6. Section 7 provides some discussions on the SNPP VIIRS geolocation, including "anomalous" events and features that may affect geolocation accuracy and possible path forwards for mitigating those anomalies. A summary and conclusions are in the last Section. Because VIIRS and MODIS instruments share many features in geometry and in the geolocation algorithm and because users around the world are familiar with more than 13 years of MODIS data, there are many references to MODIS and some experiences and results from MODIS are described for better understanding.

2. VIIRS Instrument Geometry

[4] The VIIRS instrument draws from heritage moderate resolution instrument designs of MODIS, AVHRR, SeaWiFS and OLS. VIIRS scans the Earth in the cross-track direction by using a rotating telescope assembly (RTA). Incoming rays are derotated by a half angle mirror (HAM) into a fixed aft-optics assembly (AOA), that includes a visible and near infrared (VisNIR) focal plane assembly (FPA), a shortwave and midwave infrared (SWMWIR) FPA and a long-wave infrared (LWIR) FPA in a cold dewar (Figure 1) [*NASA Joint Polar Satellite System* (*JPSS*), 2011]. The physical layout of these FPAs and bands within them is schematically shown in Figure 2 [*NASA Joint Polar Satellite System (JPSS) Ground Project*, 2011]. There are 16 moderate resolution bands (M-bands), five imagery bands (I-bands), and a day-night band (DNB). The band M16 is created by time delay integrated (TDI) of two sets of detectors (M16A and M16B) in the same spectral range. Each M-band has 16 detectors, and each I-band has 32 detectors. These detectors are optically rectangular with the smaller dimension in the along-scan direction. Within the individual I- and M-bands, an aggregation scheme of 3×1 (three scan direction samples from one track direction detector), 2×1, and 1×1, respectively, in the nadir, middle, and edge of scan is employed to limit the growth of the pixels in the scan direction (Figure 3) to about the same growth rate in the track direction, a maximum size of about 2 times nadir at the end of the scan (Figure 4). The aggregation scheme is performed onboard for the single gain bands. For dual gain bands (M1–5, M7, and M13), the aggregation is performed on the ground, leaving their unaggregation raw data records products available for research.

[5] In the track direction, as shown in Figure 3, M-band radiometric readings from one and two detectors from the top and bottom of the arrays are not transmitted to the ground in the 2×1 and 1×1 aggregations zones, respectively. This so called "bow-tie deletion" approach saves downlink bandwidth. Similarly for the I-bands, radiometric readings for two and four detectors are not transmitted in the 2×1 and 1×1 aggregation zones, respectively. Figure 3 also shows the M-bands horizontal sampling intervals (HSIs) over the equator in the three aggregation zones for an 840 km sun-synchronous, near-polar orbit that has an actual altitude of
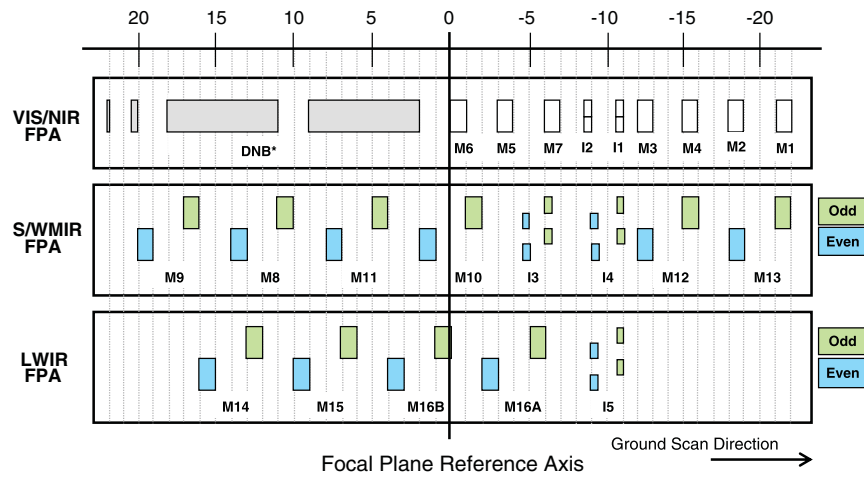

Figure 2. VIIRS band layout in the scan direction. There are 16 M-band detectors and 32 I-band detectors in the track direction. The number on top of the figure denotes band position in unit of M-band sampling intervals relative to the focal plane reference axis. The number also denotes relative number of samples dropped at the start of scan in the Earth view for alignment. DNB (*not to scale) shows four detector arrays in three gain stages. The odd and even detectors in the S/WMIR and LWIR FPAs are sampled at different times and time delayed for alignment.

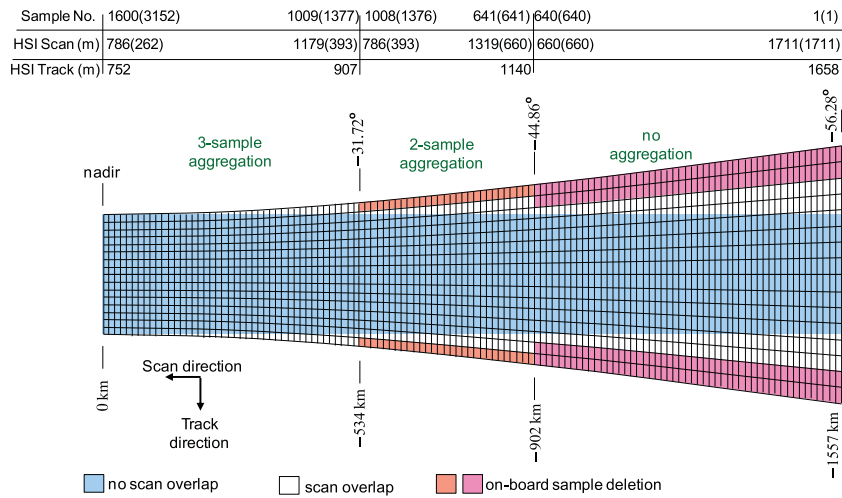| Sample No.	1600(3152)		1009(1377)	1008(1376)		641(641)	640(640)		1(1)
HSI Scan (m)	786(262)		1179(393)	786(393)		1319(660)	660(660)		1711(1711)
HSI Track (m)	752		907			1140			1658

Figure 3. SNPP VIIRS scan pattern over the Earth view for M-bands in a half scan (along-track scale is exaggerated). For I-bands, sample numbers and scan lines are doubled, while the pixel size as indicated by the HSI is half of those for M-bands. Onboard sample deletion deletes two M-band (four I-band) detectors in the two sample aggregation zone and four M-band (eight I-band) detectors in the no-aggregation zone. The numbers in parentheses for the "Sample no." and "HSI Scan (m)" are for the M-bands before aggregation.

830 km crossing the equator and varies up to 856 km over the poles. Since the VIIRS I-bands are nested into M-bands using a simple 2 × 2 approach, the HSIs for I-bands are half of those for M-bands and the number of samples in the scan direction or detector lines in the track direction are twice as many as the M-bands.

[6] The panchromatic day/night band (DNB) covers a spectrum from 0.50 μm to 0.90 μm. Its FPA shares the same optical path with the Vis/NIR FPA but uses a unique detector technology. DNB measures Earth scenes in a large dynamic range, achieved by using four charge-coupled device (CCD) arrays in three gain stages, with 250 TDI samples in high gain, three TDI samples in middle gain, and no TDI in low gain [Lee et al., 2004; Miller et al., 2012]. The band maintains a nearly constant track (scan) direction spatial resolution of 764 m (773 m) over the entire 3000 km swath using an onboard aggregation scheme. There are 32 aggregation modes, with numbers of subpixel CCD samples aggregated in the scan and track directions ranging from 66 × 42 (66 scan direction subsamples from 42 track direction cells) at nadir to 11 × 20 at both ends of a scan.

3. Summary of VIIRS Prelaunch Geometric Calibration and Characterization

[7] Intensive prelaunch geometric calibration and characterization was performed on SNPP VIIRS, both at the instrument level and spacecraft level. These measurements included sensor (detector) spatial responses, band-to-band coregistration, and pointing. This section summarizes the results relevant to on-orbit performance. Details can be found in *Fang and Puschell* [2010], *Lin et al.* [2011], and *NASA Joint Polar Satellite System* (*JPSS*) *Ground Project* [2011].

3.1. VIIRS Sensor Spatial Response

[8] The instrument sensor (detector) spatial response is system spatial impulse response for each detector as measured by its point spread functions (PSFs). Since the VIIRS detectors were fabricated to receive light in rectangular dimension in the along-scan and along-track directions, prelaunch PSFs were conveniently measured in these orthogonal two directions as line spread functions (LSFs) by using discrete, multiple thin line sources perpendicular to the LSFs
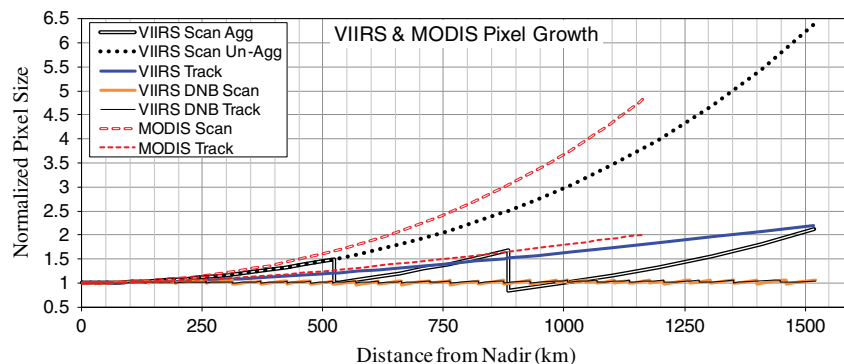
Figure 4. Pixel size growth of VIIRS bands (MODIS pixel size growth for references).
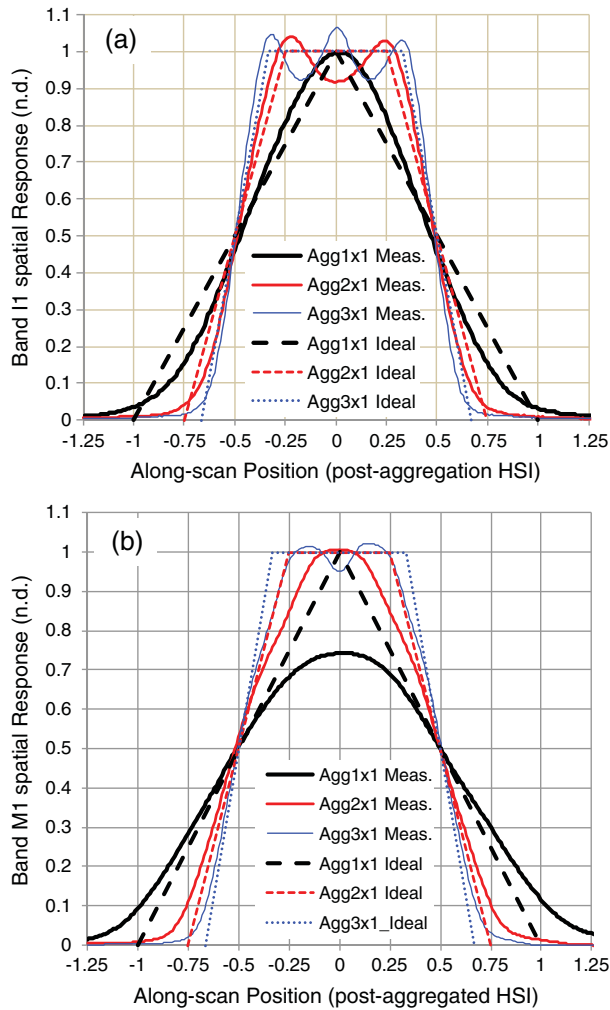
Figure 5. Prelaunch measured and ideal DLSFs in the scan direction for VIIRS bands (a) I1 and (b) M1 in three aggregation zones. Data are normalized to unity area under the curves.

to be measured. In the track direction, due to negligible spacecraft travel speed (~2%) relative to the VIIRS RTA scan speed, the LSFs were measured as static LSFs with line sources parallel to the RTA scan direction. The results of

the track LSFs are essentially squares, the size of which is dictated by the size of the detectors. The field of view (FOV) is within ±5% of HSI for all bands except for a few detectors in band I5 and a known underperforming edge detector in band M12 [*Lin et al.*, 2011], which is not used in 2 × 1 and nonaggregation zones due to bow-tie deletion.

[9] In the scan direction, the VIIRS telescope rotates an angular sampling interval during each temporal sampling interval, the majority of which is the sampling integration time. This results in a detector's static or instantaneous LSF to be "dragged" along the scan direction, and a dynamic LSF (DLSF) is formed. The shape of the DLSF is trapezoidal based, with the edges blurred by the instrument optical PSF. Figure 5 shows two typical examples of DLSFs in the scan direction for bands I1 and M6. The LSFs for 3 × 1 and 2 × 1 sample aggregation zones are constructed from the measured DLSF in the diagnostic mode, e.g., nonaggregation ("Agg1×1") without bow-tie deletion. The "ideal" DLSFs are shown here as references, of which band I1 are used in geolocation error trending and correction discussed in section 5.

[10] The performance parameters are obtained from the DLSFs. One important parameter is the full width at half maximum of the DLSFs, which is a measure of the footprint and sometimes is called dynamic FOV (DFOV). Figure 6 shows the DFOVs in the along-scan direction in all aggregation zones from the nominal performance temperature plateau at the thermal vacuum testing before launch. We see that we have undersampling for all I-bands in all aggregation zones and oversampling for all M-bands in the nonaggregated zone. As we move closer to the nadir in the 2 × 1 and 3 × 1 aggregation zones, the footprint sizes are closer to pixel sizes, and all M-band footprint sizes are nearly identical to pixel sizes. Note that the prelaunch test results of footprint sizes are equivalent to those of the top of atmosphere observations.

3.2. VIIRS Band-to-Band Coregistration

[11] Band-to-band coregistration (BBR) is crucial for multiple spectral bands remote-sensing instruments such as VIIRS that use signals from multiple bands to retrieve environmental data records. The BBR is defined as the overlap of point spread functions (PSFs) from one detector in one
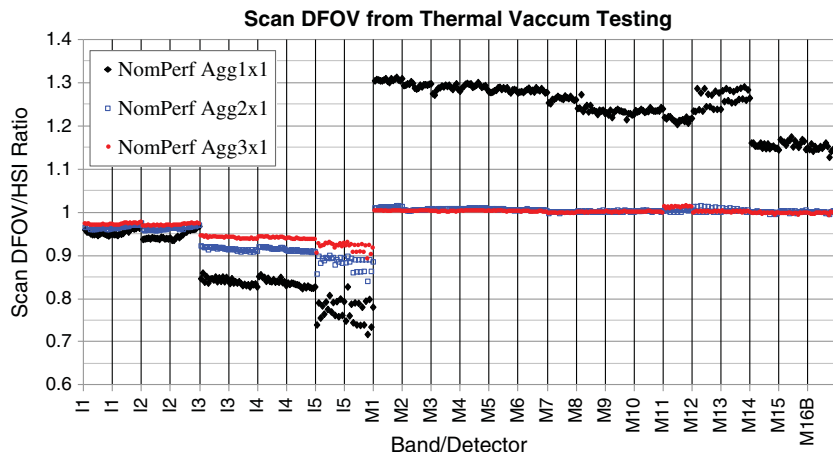

Figure 6. Scan DFOV in three aggregation zones (each point represents a detector).
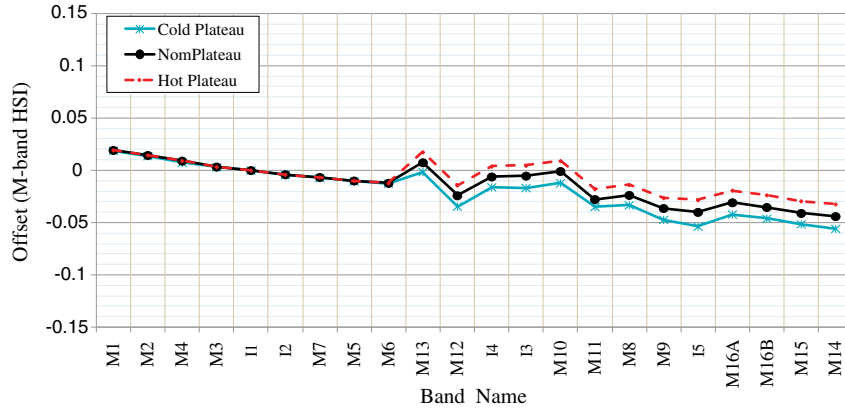
Figure 7. VIIRS along-track band offset results from TVac testing (relative to band I1) combined with the effects of on-orbit spacecraft travel velocity. Along-scan sample aggregation effect is negligible.

spectral band to a corresponding detector in another spectral band. For the on-orbit operations, the interest is focused on the offsets in the band-averaged relative location. Since the geolocation of band I1 is calibrated on-orbit, as described in section 5, the relative offsets of other bands are compared to this band with accurate measurements on the ground testing, as plotted in Figures 7 and 8. The ground testing used a diagnostic mode that is equivalent to the unaggregated 1×1 zones. Figure 8 also shows the improved coregistration in the 2×1 and 3×1 aggregation zones. In the ground thermal vacuum (TVac) testing, the "cold" and "hot" plateaus were used to simulate early and late on-orbit conditions in space. The "nominal" plateau is a representative of general on-orbit conditions.

[12] Note that since the geolocation is performed based on registration of a single band to the ground control points, the exact location of the other bands can be calculated independently using prelaunch measurements of the BBR offsets (section 6.4) or the other bands' BBR offsets can be considered an additional geolocation error for those bands. Even if the prelaunch BBR measurements are used, there may be additional errors in the geolocation because the on-orbit BBR may have changed from the prelaunch measurements. However, prelaunch data and on-orbit lunar measurements (section 6.4) indicate that these BBR offsets are small (~0.1 M-band HSI or ~75 m).

3.3. VIIRS Pointing and Alignments

[13] Alignment of various VIIRS optical components have been intensively measured and adjusted at the sensor integration level and the instrument pointing measured at the sensor level. The overall alignment of the instrument to the spacecraft was made at the spacecraft integration level. VIIRS instrument to spacecraft alignment on the ground is summarized as follows:

[14] 1. A master alignment cube (MAC) was attached to the spacecraft, and an optical cube was attached to the VIIRS instrument.

[15] 2. The Alignment between the spacecraft MAC and VIIRS optical cube was checked and corrected as necessary by using an array of fine resolution (precise to 1 arc sec) theodolites.

[16] 3. The two star trackers on the spacecraft were aligned with the spacecraft coordinate system, which is linked to the attitude determination and control subsystem (ADCS). The attitude control frame points to the Earth geodetic nadir.

[17] 4. The alignment between the VIIRS optical cube and the VIIRS Mechanical Axis (VMA) was measured. The VMA is used as the internal reference frame for the instrument's optical components.

[18] The relationship between these measurements and their coordinate systems is illustrated in Figure 9. In addition to this overall alignment, prior to spacecraft integration, during the integration and ground testing of VIIRS, precise
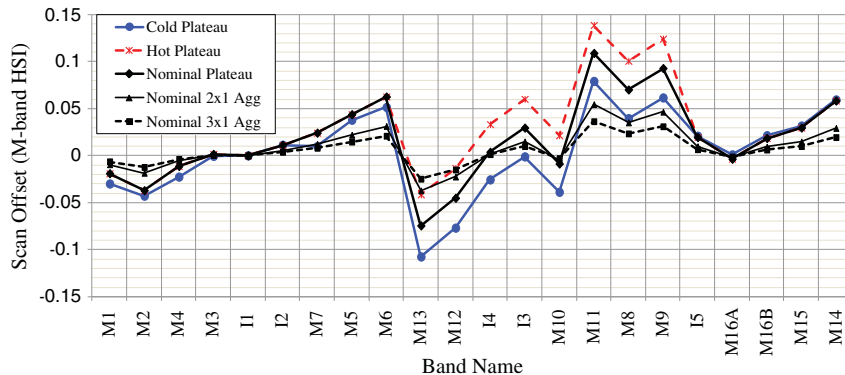

Figure 8. VIIRS along-scan band offset results from TVac testing (relative to band I1). The effects of along-scan sample aggregation are shown for the nominal plateau case.
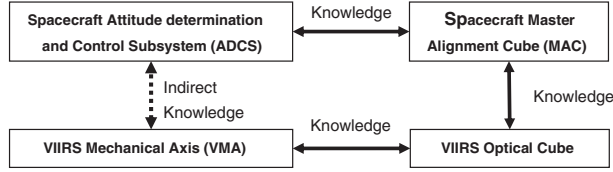
Figure 9. Illustration of indirect alignment between the VIIRS VMA and the spacecraft ADCS reference frames.

measurements were made of individual VIIRS components (e.g., HAM), which are used in the VIIRS geometric model in the geolocation algorithm. No VIIRS optical components are adjustable after launch.

4. VIIRS Geolocation Algorithm

[19] The VIIRS geolocation algorithm is based on models of the instrument, spacecraft orbit, and the Earth. This section briefly outlines the algorithm in its components, listing of coordinate transformations, pictorial views of pointing from detectors on focal planes through HAM and RTA, and the mathematical expression of the view vector from detector to the Earth surface through HAM and RTA.

4.1. Algorithm Components

[20] VIIRS geolocation algorithm includes a geometric parameterization of the following components: (1) detectors and focal plane in the aft optical system, (2) rotating half angle mirror system (HAM), (3) rotating telescope system (RTA), (4) spacecraft coordinate system, (5) instrument coordinate system, (6) orbital coordinate system, (7) Earth-centered Inertial (ECI) coordinate system (J2000), (8) Earth-centered Earth Fixed coordinate system (ECEF) (also known as Earth-Centered Rotating Coordinate system), and (9) Earth ellipsoid and geoid with or without a terrain model.

4.2. Coordinate Transformations

[21] The line of sight of the center of each detector is modeled as a vector that starts at the focal plane and goes through aft optical system, HAM, and RTA to produce a vector in the instrument reference frame. At each stage, a transformation matrix transforms the vector's coordinate system based on the knowledge of the optical components and their positions at the time of each sample. Then using knowledge of the instrument alignment and spacecraft position and attitude the Earth location (geolocation) where this look vector intersects the Earth's surface is computed. Specifically, the following steps are performed (Figure 10):

[22] 1. Starting with the detector vector (x,y,f), where (x,y) is detector position in a focal plane and f the aft-optics focal length, transform it from the aft-optics to the HAM reference frame.

[23] 2. Based on the HAM mirror side and angle determined by encoder data, reflect the vector off the HAM mirror and then rotate to the RTA reference frame.

[24] 3. Based on the RTA angle determined by encoder data, the vector is magnified and rotated to the RTA output frame. RTA and HAM are synchronized, and the HAM rotation rate is one half of RTA's.
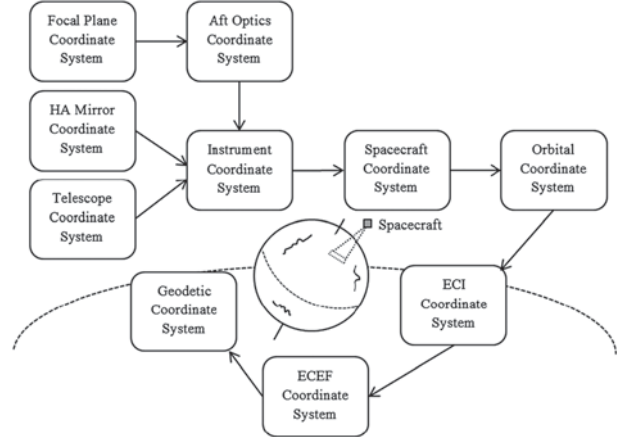

Figure 10. Coordinate systems used in VIIRS pointing and geolocation algorithm.

[25] 4. The vector from the RTA is converted to the spacecraft coordinate system by using the instrument to spacecraft alignment information.

[26] 5. The spacecraft position and velocity is used to determine the orbital coordinate system, where the original spacecraft position in ECEF must be converted to ECI.

[27] 6. The vector leaves spacecraft according to spacecraft attitude and transformed into the orbital coordinate system.

[28] 7. The vector in the orbital frame is then rotated to ECI and then in ECEF.

[29] 8. Using the look-point equation, the pierce point is computed for both the ellipsoid Earth and the Earth's actual surface modeled with a digital elevation model (DEM).

4.3. Pointing Through Focal Planes, HAM, and RTA

[30] Figures 11 and 12 show the relationships between the aft optics, HAM, and RTA when the RTA is pointing toward nadir. In these figures, the following are defined:

X_A, Y_A, Z_A – aft-optics coordinate system
X_H, Y_H, Z_H – HAM coordinate system
X_T, Y_T, Z_T – RTA coordinate system
$\mathbf{n}_{side1}, \mathbf{n}_{side2}$ – normal vectors to the HAM mirror sides
$\mathbf{o}_{inX}, \mathbf{o}_{inY}, \mathbf{o}_{inZ}$ – RTA entrance basis vectors
$\mathbf{o}_{outX}, \mathbf{o}_{outY}, \mathbf{o}_{outZ}$ – RTA exit basis vectors
ω_T, ω_H – RTA and HAM angular velocity
Ω_T – telescope entrance angle (nominally 61.5°)
θ_A – Aft-optics along-scan angle (nominally 44°)
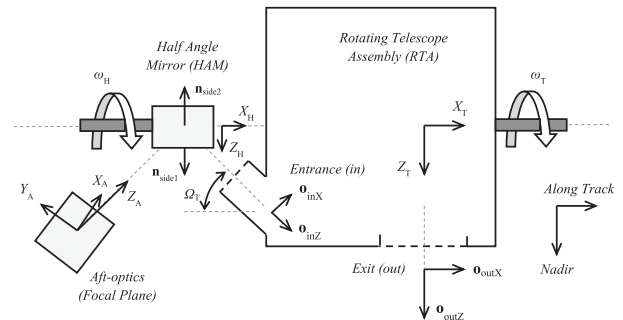θ_H – HAM angle

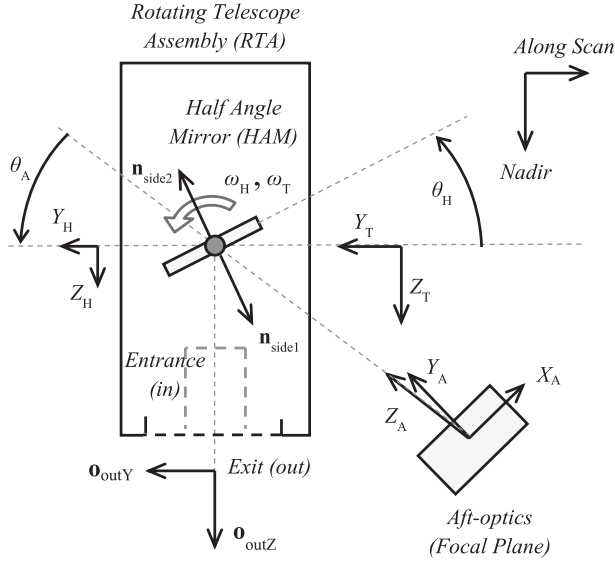**Figure 11.** Side view of RTA and HAM when pointing at nadir.

Figure 12. Front view of RTA and HAM when pointing at nadir.

[31] Both the RTA and HAM are synchronized, and when RTA is pointing to nadir, the HAM is nominally pointing 23° off nadir, as in Figure 12. Also, the HAM rotates at half the speed of the RTA (this is the meaning of the term "half angle" mirror).

4.4. View Vector From Focal Plane to the Earth Surface Through HAM/RTA

[32] The following steps are needed to compute the location on the Earth surface of the center of a detector at the midpoint of the sample integration time:

[33] 1. The HAM normal vector $\hat{\mathbf{n}}_{\mathrm{mirr}}$ in the instrument coordinate system is computed using the mirror rotation matrix $\mathbf{T}_{\mathrm{rot}}(\theta)$ with rotation angle θ_{H}, HAM to instrument alignment matrix $\mathbf{T}_{\mathrm{inst/H}}$, and appropriate HAM side normal vector $\hat{\mathbf{n}}_{\mathrm{side}i}$ by

$$\hat{\mathbf{n}}_{\mathrm{mirr}} = \mathbf{T}_{\mathrm{inst/H}}\,\mathbf{T}_{\mathrm{rot}}(\theta_H)\,\hat{\mathbf{n}}_{\mathrm{side}i} \tag{1}$$

where the rotation matrix $\mathbf{T}_{\mathrm{rot}}(\theta)$ is expressed by

$$\mathbf{T}_{\mathrm{rot}}(\theta) = \begin{bmatrix} 1 & 0 & 0 \\ 0 & \cos(\theta) & -\sin(\theta) \\ 0 & \sin(\theta) & \cos(\theta) \end{bmatrix} \tag{2}$$

The HAM rotation angle $\theta_{\mathrm{H}} = A_0^{\mathrm{H}} + A_1^{\mathrm{H}} n_{\mathrm{encH}}$ is computed by two coefficients (A_0^{H} and A_1^{H}) and the HAM encoder count n_{encH} at the midpoint of the sample integration time.

[34] 2. The vector $\mathbf{u}_{\mathrm{H}}$ coming from a detector center location on the focal plane (via the aft optics) in the instrument coordinate system toward the HAM is reflected by HAM and becomes the vector $\mathbf{u}_{\mathrm{tel}}$ using the following equation:

$$\mathbf{u}_{\mathrm{tel}} = \mathbf{u}_{\mathrm{H}} - 2\,\hat{\mathbf{n}}_{\mathrm{mirr}}(\mathbf{u}_{\mathrm{H}}{\cdot}\hat{\mathbf{n}}_{\mathrm{mirr}}) \tag{3}$$

[35] 3. The next step is to pass through the rotating telescope at angle θ_{T}. This is done by using rotation matrices $\mathbf{M}_{\mathrm{in}}(\theta_{\mathrm{T}})$ and $\mathbf{M}_{\mathrm{out}}(\theta_{\mathrm{T}})$ constructed from the entrance and exit vectors of the telescope including the magnification $\mathbf{M}_{\mathrm{mag}}$ by the telescope:

$$\mathbf{u}_{\mathrm{inst}} = \mathbf{M}_{\mathrm{out}}(\theta_T)\,\mathbf{M}_{\mathrm{mag}}\mathbf{M}_{\mathrm{in}}(\theta_T)\,\mathbf{u}_{\mathrm{tel}} \tag{4}$$

The RTA rotation angle $\theta_{\mathrm{T}} = A_0^{\mathrm{T}} + A_1^{\mathrm{T}} n_{\mathrm{encT}}$ is computed by two coefficients (A_0^{T} and A_1^{T}) and the RTA encoder count n_{encT} at the midpoint of the sample integration time. The telescope entrance and exit basis vectors $[\mathbf{o}_{\mathrm{inX}}\ \mathbf{o}_{\mathrm{inY}}\ \mathbf{o}_{\mathrm{inZ}}]$ and $[\mathbf{o}_{\mathrm{outX}}\ \mathbf{o}_{\mathrm{outY}}\ \mathbf{o}_{\mathrm{outZ}}]$ are used to construct the telescope rotation matrices using the RTA to instrument alignment matrix $\mathbf{T}_{\mathrm{inst/T}}$ by

$$\mathbf{M}_{\mathrm{in}}(\theta_T) = \mathbf{T}_{\mathrm{inst/T}}\mathbf{T}_{\mathrm{rot}}(\theta_T)\,[\mathbf{o}_{\mathrm{inX}}\ \mathbf{o}_{\mathrm{inY}}\ \mathbf{o}_{\mathrm{inZ}}] \tag{5}$$

$$\mathbf{M}_{\mathrm{out}}(\theta_T) = \mathbf{T}_{\mathrm{inst/T}}\mathbf{T}_{\mathrm{rot}}(\theta_T)\,[\mathbf{o}_{\mathrm{outX}}\ \mathbf{o}_{\mathrm{outY}}\ \mathbf{o}_{\mathrm{outZ}}] \tag{6}$$

The RTA magnification matrix $\mathbf{M}_{\mathrm{mag}}$ is computed from the telescope magnification factor m (nominally 4.0):

$$\mathbf{M}_{\mathrm{mag}} = \begin{bmatrix} \dfrac{1}{m} & 0 & 0 \\ 0 & \dfrac{1}{m} & 0 \\ 0 & 0 & 1 \end{bmatrix} \tag{7}$$

[36] 4. The view vector $\mathbf{u}_{\mathrm{inst}}$ in the instrument coordinate system is then rotated to an Earth fixed coordinate using the instrument to spacecraft alignment matrix $\mathbf{T}_{\mathrm{sc/inst}}$, the spacecraft attitude data (*roll, pitch, yaw*) to convert to the orbital reference frame $\mathbf{T}_{\mathrm{sc/inst}}(roll, pitch, yaw)$, and the spacecraft position and velocity $(\mathbf{p,v})$ to convert to the system the moving Earth coordinate system $\mathbf{T}_{\mathrm{ecef/orb}}(\mathbf{p,v})$ by

$$\mathbf{u}_{\mathrm{ecef}} = \mathbf{T}_{\mathrm{ecef/orb}}(\mathbf{p}, \mathbf{v})\,\mathbf{T}_{\mathrm{orb/sc}}(roll, pitch, yaw)\,\mathbf{T}_{\mathrm{sc/inst}}\mathbf{u}_{\mathrm{inst}} \tag{8}$$

Figure 13. (left) Over 1200 Landsat-based ground control point chips distributed globally and (right) a sample chip around Appleton, Wisconsin, from Landsat 5 observed on 8 November 1999.
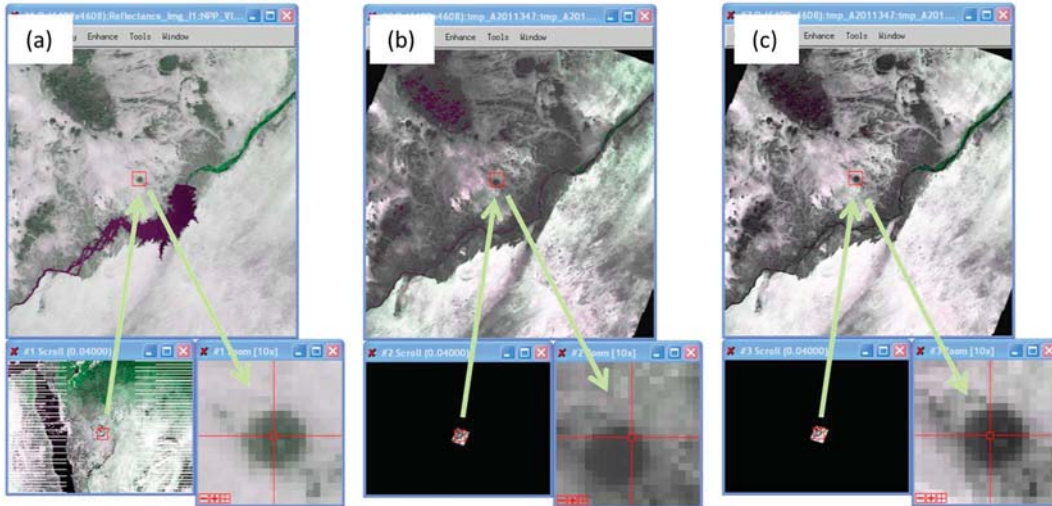
Figure 14. Illustration of the process to double check the first VIIRS on-orbit geolocation error correction via LUT update as explained in the text. (a) VIIRS band I1 image acquired on 13 December 2011. The center of a circular patch is in Sudan, Africa (18.68°N, 32.29°E). (b) Simulated image from Landsat chip using the geolocation of the VIIRS image. (c) Simulated image using updated geolocation.

[37] 5. From the spacecraft position **p** (in ECEF coordinates), the view vector $\mathbf{u}_{ecef}$ points toward the Earth and determines a pierce point on the surface of the terrain using the look-point equation and terrain correction algorithm.

[38] The RTA and HAM encoder to angle conversion coefficients as well as other instrument model constants are stored in the geolocation lookup table. Additional algorithm details may be found in *Wolfe et al.* [2002] and *NASA Joint Polar Satellite System* (*JPSS*) *Ground Project* [2011]. The results of the algorithm are presented in the next section.

5. VIIRS Geolocation Error Correction and Trending

[39] Geolocation errors are measured, corrected, and trended by a control point matching (CPM) program that has been used for more than 13 years to successfully characterize and correct MODIS geolocation errors [*Nishihama et al.*, 1997; *Wolfe et al.*, 2002; *Wolfe et al.*, 2006; *Wolfe and Nishihama*, 2009]. The program has been adapted for VIIRS to accommodate its geometric features of sample aggregation and bow-tie deletion schemes as described in section 2. The CPM program uses Landsat red band 30 m resolution 800 by 800 pixel clear subscenes, which are called ground control point chips. Over the years, we have developed a library of over 1200 chips distributed globally from Landsat 4, Landsat 5, and Landsat 7 (Figure 13). We will continue to develop and upgrade the library from recently launched Landsat 8, i.e., the Landsat Data Continuity Mission. For VIIRS, these chips are used to simulate images of VIIRS band I1 375 m nadir resolution with their corresponding projection of idealized LSFs in triangle or trapezoidal (cf. Figure 5) shape in the scan direction and evenly distributed in the track direction. The simulated images are then correlated with VIIRS images. The shifts of the control points at maximum cross correlation form a series of control point residuals. These residuals are analyzed for corrections of various sensor parameters in the geolocation algorithm

lookup table (LUT). This process coregisters VIIRS band I1 to the Landsat red band. The geolocation of all other VIIRS M- and I-bands are tied to I1 through BBR (cf. section 3.2). Because the ground sample distance varies over the scan, the geolocation accuracy is reported in nadir equivalent units.

[40] In the first 3 weeks after launch, the SNPP spacecraft and instruments went through early orbit checkout. The nominal altitude of the satellite was attained on 16 November 2011. The onboard attitude determination and control subsystem (ADCS) was calibrated and tuned on 17 November 2011. The VIIRS nadir door was opened on 21 November 2011, making the VisNIR bands available for geolocation accuracy assessment. The cryoradiator door was opened on 18 January 2012, to cool down the cold FPAs for observations in all spectral bands.

[41] We began by analyzing the VIIRS visible data collected on 13 December 2011 using the CPM program. Even though the alignment of the instrument to the spacecraft was well characterized before launch, accelerations that occurred during launch could have shifted the instrument relative to the spacecraft so that an initial on-orbit bias adjustment was necessary. The CPM program is run at the NASA SNPP Science Data Segment (SDS) Land Product Evaluation and Testing Element (PEATE). Initially, a CPM step size of 0.2 I1 sampling intervals was used. Based on the residuals from this day, the first on-orbit geolocation lookup tables (LUTs) were updated that corrected the instrument to spacecraft alignment matrix. Then the CPM step size was refined to 0.05 I1 sampling intervals and has remained so since then, to fine-tune and confirm the changes.

[42] Figure 14 illustrates a process checking the first VIIRS on-orbit geolocation error correction via a LUT update using a Landsat Thematic Mapper (TM) scene. In order to see how closely the corrected geolocation is to the observed location on the ground, a program was developed to simulate the VIIRS radiance from the TM scene by applying the first-order VIIRS LSF to a TM scene based on the VIIRS geolocation. To

Table 1. VIIRS Geolocation Parameter Updates

Parameter (arc sec)	At Launch (12 December 2011)	First Update (23 February 2012)	Second Update (18 April 2013)
inst_roll	33.2	−227.3	−227.3
inst_pitch	41.2	153.2	66.4
inst_yaw	−59.3	95.4	74.4
ham_alpha	3.9	3.9	3.6
ham_beta	9.5	9.5	9.5
ham_gamma	−6.0	−6.0	−6.2
ham_roll	0.0	0.0	21.8
ham_pitch	0.0	0.0	79.7
ham_yaw	0.0	0.0	38.8
tele_roll	0.0	0.0	0.0
tele_pitch	0.0	0.0	65.9
tele_yaw	0.0	0.0	11.0

compare with a real VIIRS image, the I1 band image is used. A selected area over Sudan is shown in Figure 14a (the image is flipped so that the top of the image is south). A target point in the center of the circular feature was selected for this example, and the location (sample, line) of the pixel was extracted. Figure 14b shows that before geolocation parameter LUT update the simulated image shows that the target point is not in the center of the circular feature. Figure 14c shows that after LUT was updated, the target point in the simulated image is located close to the center of circular feature, as it is in the real image in Figure 14a. This illustrates how the updated geolocation points to the true VIIRS' pointing. By comparing between the close-up images in Figures 14a and 14c, any remaining shift can be seen.

[43] The first on-orbit updated LUTs removed geolocation biases in the nadir equivalent units of −775 m in the track direction and 1118 m in the scan direction, which were put into operations on 23 February 2012. A similar process was performed by a Northrop Grumman (NG) team to update DNB geolocation parameter LUT on 30 March 2012 that further removed 1.3 km nadir equivalent bias in the scan direction for DNB geolocation by shifting DNB detector position on the focal plane. A refined update of the DNB geolocation parameter LUT by the same NG team made the geolocation accuracy closer to the truth by about 340 m nadir equivalent in the scan direction on 15 February 2013. After more than 1 year of operations, a multiparameter geolocation LUT refinement was put in operations on 18 April 2013 to remove systematic scan-angle dependent bias in the track direction and long-term

temporal biases in the track and scan directions. This update also included a small A-side Scan Control Electronics (SCE) coefficient adjustment. Table 1 shows the LUT updates, including the last two updates that greatly improved the geolocation accuracy, as showed in Table 2.

[44] The temporal trends of the geolocation errors are shown in Figure 15, with accuracies after the second on-orbit corrections (based on Land PEATE reprocessing). Between the first and second LUT updates, the SCE was switched from side-B to side-A on 22 November 2012. After the switch, it was found that coefficients for the side-A encoders were erroneously set, which caused a geolocation error of about 325 m in the scan direction. That error was corrected on 11 December 2012. More details about the event will be discussed in section 7.

[45] The scan-angle dependent geolocation errors are shown in Figure 16, with the accuracies after the second on-orbit corrections (based on Land PEATE reprocessing). In the scan direction, a small oscillation persists that may be related to the encoder. We are continuing to work to better understand the source of this irregularity.

[46] We have examined sun angle dependent geolocation errors from the reprocessed data. We are happily surprised that no obvious trends of sun angle dependent geolocation errors are found from the 16 months VIIRS on-orbit operations data. This means that no obvious thermal distortion is detected so far, contrary to the prelaunch predictions [*Lin et al.*, 2011]. We will keep an eye on these trends, as MODIS geolocation errors have strong correlations with sun angle and have to be corrected [*Wolfe and Nishihama*, 2009].

[47] As we can see from the last two columns in Table 2, the geolocation accuracy of VIIRS and MODIS are similar relative to their respective pixel sizes. The values in the table are described in nadir equivalence units. The errors grow as the observations are away from the nadir point to the ends of scan. The growth rates in the track and scan directions are depicted respectively as the "VIIRS Track" and "VIIRS Scan Un-Agg" curves in Figure 4. This is true for band I1. For other I-bands and M-bands, there are small offsets from band I1, as depicted in Figures 7 and 8 in the BBR subsection.

[48] For the DNB, geolocation is only computed using an ellipsoidal Earth model without terrain correction. This is different from the I- and M-bands for which both ellipsoid geolocation and terrain corrected geolocation are provided.

Table 2. VIIRS Geolocation Accuracy (MODIS Data for Comparison)

Residuals	At Launch 12 December 2011	First Update 23 February 2012	Second Update 18 April 2013	MODIS Aqua (C6)
Track mean	−755 m, −201%[a]	−24 m, −7%	2 m, 1%	1 m, 0%
Scan mean	1118 m, 298%	−8 m, −2%	2 m, 1%	1 m, 0%
Track RMSE	782 m, 209%	75 m, 20%	70 m, 19%	46 m, 18%
Scan RMSE	1120 m, 299%	62 m, 17%	60 m, 16%	51 m, 20%
Data days	1	408[c]	461[d]	3,539
Matchups/day	97[b]	133	137	228

[a]Percentage (%) is based on a nadir pixel size of 375 m for VIIRs and 250 m for MODIS.
[b]This matchup value was before the first update using step size of 0.2 I-band pixel.
[c]The statistics after the first on-orbit updated excluded 19 data days after the Scan Control Electronics (SCE) was switched from B-side to A-side on 22 November 2012 and before the encoder coefficients were corrected on 11 December 2012. Also, data days before the first update were not included, starting from 19 January 2012 to 22 February 2012.
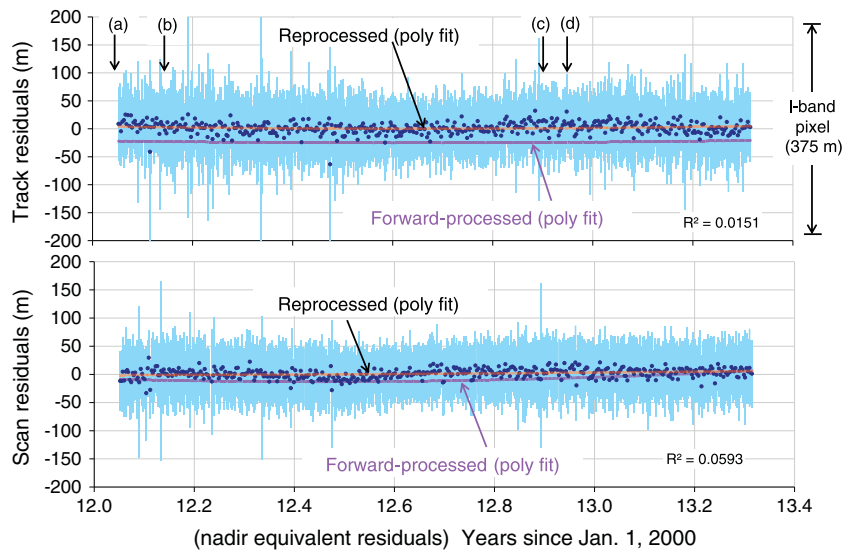[d]The statistics include data reprocessed starting from 19 January 2012 to 27 April 2013.

Figure 15. Trends of geolocation errors in the (top) track and (bottom) scan directions. Solid circles are the daily mean, and the light vertical bar is the daily standard deviation (nadir equivalent units). Polynomial fitted lines for the forward-processed data and I-band pixel size are marked for references. Four events are marked in Figure 15 (top): start of reprocessing on 19 January 2012 (a), the first on-orbit geolocation parameter LUT update for forward processing on 23 February 2012 (b), the Scan Control Electronics (SCE) switch from B to A side on 22 November 2012 that caused geolocation error of −325 m in the scan direction in the forward-processing data (not shown here and not used for the polynomial fit) (c), and the coefficients for SCE A side updated on 11 December 2012 that corrected the geolocation error (d).

Terrain corrected geolocation uses a digital elevation model (DEM) to correct for the terrain parallax introduced by VIIRS at large off-nadir scan angles. The error factor without terrain correction is a function of scan angle, and it is a maximum of 2.75 at the end of a scan. Multiplying this factor by the elevation gives the geolocation error in the scan direction caused by ignoring the terrain. For example, when Mount Everest (8.85 km) is viewed at the end of the scan, there is a 24.3 km difference between the ellipsoid and terrain corrected geolocation (the terrain corrected location is closer to nadir). Even in the oceans or at the coastlines, mean sea level (geoid) may be off up to 107 m from the ellipsoid Earth model, which could results in a 300 m geolocation error at the end of scan.

[49] We have developed software for terrain corrected geolocation for DNB by reusing the code for computing
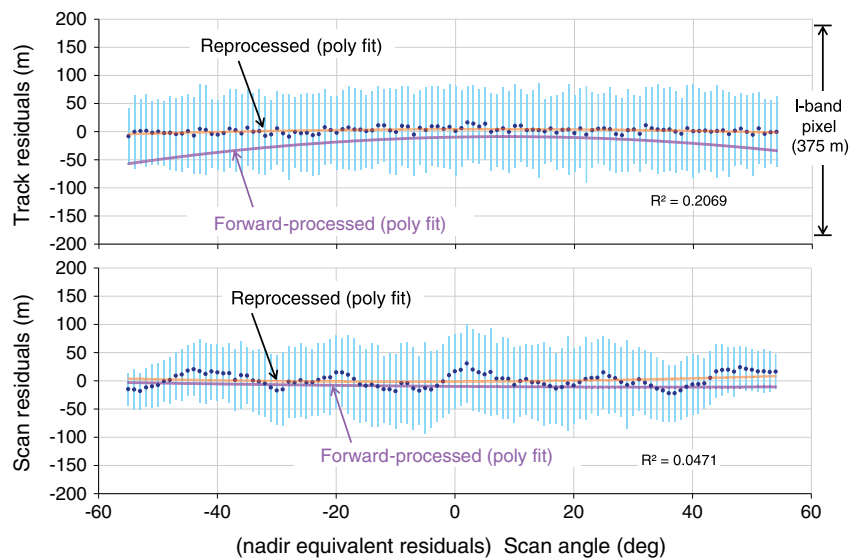

Figure 16. Scan angle dependent geolocation errors in the (top) track and (bottom) scan directions. Solid circles are the bin averages every 1°, and the light vertical bars are the standard deviations within bins (nadir equivalent units). Polynomial fitted lines for the forward-processed data and I-band pixel size are marked for references.
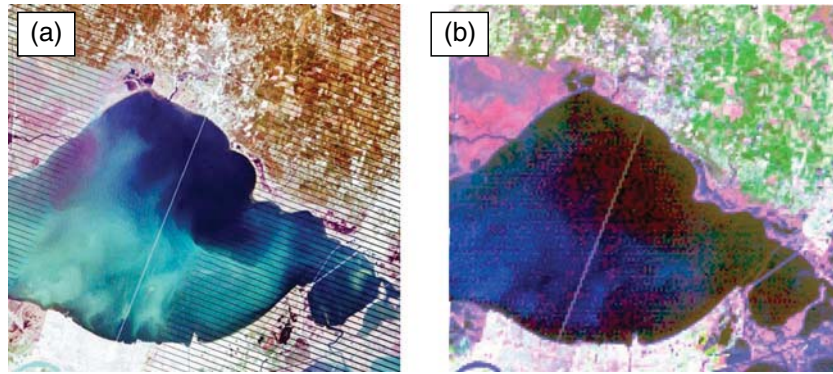
Figure 17. Lake Ponchartrain subsets for (a) Landsat 7 on 21 November 2012 and (b) NPP VIIRS image on 20 November 2012. The images are cogeolocated using the available geolocation information. In both cases, bands 3, 2, and 1 are displayed as red, green, and blue, respectively, and displayed with histogram equalization. The stripes in the Landsat 7 image are a manifestation of Scan Line Corrector Failure [*Storey et al.*, 2005].

I-band geolocation. This has been implemented at NASA Land PEATE, and the production started on 13 May 2013 for data acquired after 00:00Z, 13 May 2013. On the same day, Land PEATE also started reprocessing sensor data records, including terrain corrected only I-band, M-band, and DNB geolocaiton products, for data acquired from 00:00Z on 19 January 2012, shortly after the cryoradiate door was opened 18 January 2012, by using the most updated software and LUTs. These LUTs include the geolocation parameter LUTs updated on 18 April 2013 and definitive radiometric LUTs from January 2012 to May 2013 that capture the temporal variations due to the SNPP VIIRS RTA mirror degradation [*Xiong et al.*, 2013].

6. VIIRS On-Orbit Geometric Characterization

[50] Besides the on-orbit geolocation error correction and trending described in section 5 above, other geometric performance has also been characterized. These include the characteristics of the spacecraft ephemeris and attitudes, on-orbit BBR and on-orbit sensor spatial response characterizations.

6.1. Spacecraft Ephemeris and Attitudes

[51] The SNPP satellite with VIIRS and other instruments onboard has an 840 km, sun-synchronous, near-polar orbit with inclination of 98.7 degrees and nominal equatorial local crossing time of $13:30 \pm 10$ min. The orbital period is 101.5 min, and it has a repeat cycle of 16 days. The altitude is at its lowest of 828 km over the equator and highest of 856 over the South Pole, with mean altitude of 840 km. The velocity is at its fastest when crossing the equator. That combination makes the equatorial region most stringent for scan-to-scan contiguity, for which the current SNPP VIIRS has no underlap. Also the orbit-to-orbit swaths have the smallest overlap of about 10% in the equatorial area. Trending of ephemeris data shows that the orbit has been tightly controlled by Delta-V drag makeup maneuvers, with the equatorial crossing altitude fluctuating within 1 km of 829.8 km and the equatorial crossing speed fluctuating within 1 m/s of 7535.8 m/s. The equatorial crossing local time has a small variation. It was at 13:25:24 when the SNPP attained nominal altitude on 17 November 2011. It slowly moved

to the west at 13:23:02 (a 66 km drift on the ground) on 1 November 2012 and then back eastward to 13:24:05 as of 12 May 2013.

[52] Along with the ephemeris data, the spacecraft attitude data are reported in the spacecraft telemetry (also known as housekeeping data) at once a second. In general,
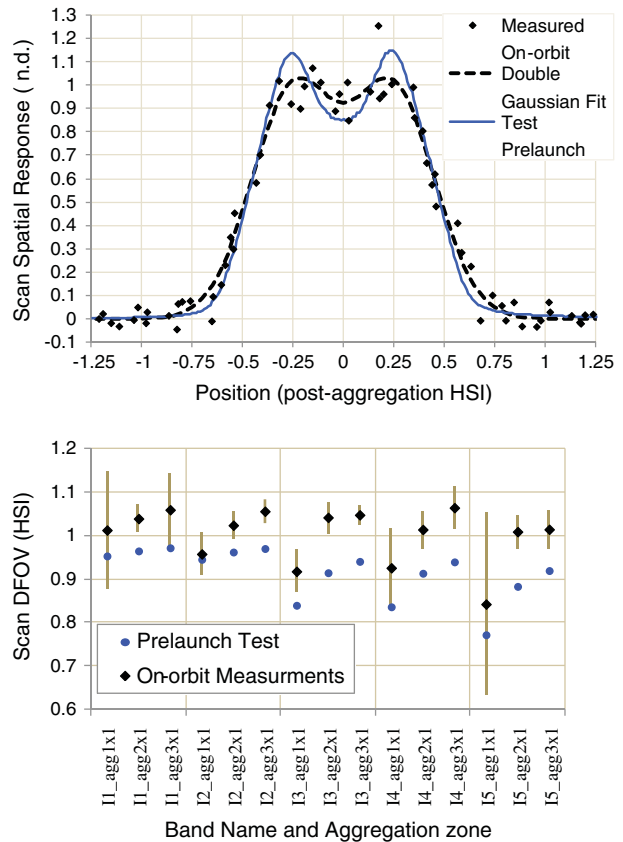

Figure 18. (top) An example of constructed LSF for band I3 in Agg2x1 zone. (bottom) Results of the DFOV measured in the scan direction for the I-bands (solid diamond for the mean, bar for the standard deviation, and the solid circle from the prelaunch test (cf. Figure 6).
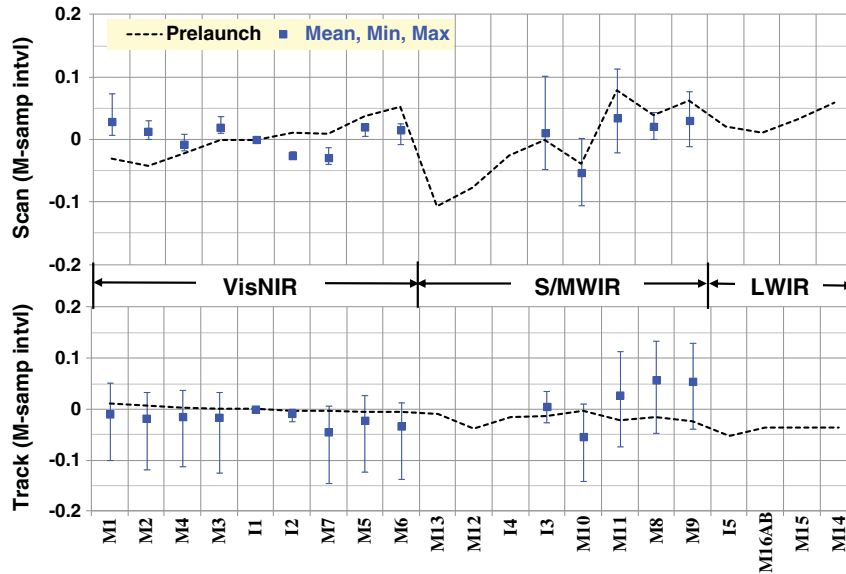
Figure 19. Band-averaged (top) scan and (bottom) track spectral band registration (relative to band I1) from the five lunar calibration maneuvers up to 31 May 2012 compare well with prelaunch testing.

there are slow orbital variations in roll and yaw in amplitudes of about 15 arc sec and semiorbital variation in pitch in amplitude of about 5 arc sec. The attitude variations are tracked by ground geolocation software, except for those high-frequency (greater than 0.5 Hz) variations since the geolocation software interpolates between the attitude that is downlinked once a second.

6.2. On-Orbit RTA/HAM Encoder Characterization

[53] VIIRS uses a scan control electronic assembly (SCE) that uses encoders to control the rotating telescope assembly (RTA) and half angle mirror (HAM) motors. The SCE maintains the nearly constant speed of the RTA at 3.531 rad/s and the HAM at 1.766 rad/s. Some nonlinearity exists [*Wolfe et al.*, 2012], which is tracked and removed in the ground geolocation software. The SCE also synchronizes the relative position of the RTA and HAM so that when the RTA views various sectors, the incoming rays are directed to the detectors within the AOA in an appropriate time for digitization, storage, and transmission to the ground. When the RTA and HAM are synchronized, the variation in the start of scan in one scan to the next in the Earth View sector is small [*Wolfe et al.*, 2012], which is also tracked in the ground software for proper geolocation. However, if the motions of RTA and HAM are not in sync, the variations become large and this results in improper geolocation. For VIIRS, this synchronization loss is very rare, but it does occur and is further discussed in section 7.

6.3. On-Orbit Sensor Spatial Response Characterization

[54] VIIRS on-orbit spatial response is expected to be similar to the measurements from the ground testing as MODIS has shown us with its onboard spectroradiometric calibration assembly [*Xiong et al.*, 2005; *Xiong et al.*, 2006]. For VIIRS, there is no onboard spatial characterization capability, but the Pontchartrain Causeway near New Orleans in Louisiana provides a convenient

linear ground target, although atmosphere induced blur is included in the measurement. Figure 17 displays the cogeolocated Landsat 7 Thematic Mapper (TM) and SNPP VIIRS data sets from 21 and 20 November 2012, respectively. Using finer than Landsat resolution (30 m) grid to model both the Landsat and VIIRS scenes enables us to extract and construct LSF for the VIIRS in the along-scan direction for all three aggregation zones in cloud free conditions. Figure 18a shows an example of constructed LSF for band I3 in the 2 × 1 aggregation zone and double Gaussian fitted curve (we use Gaussian function to model preaggregated along-scan LSF). The results of DFOV in the scan direction for the five I-bands are shown in Figure 18b, which are consistent with results from prelaunch tests, considering the effects of atmospheric modulation [*Buskila et al.*, 2004], nonuniformities of water surface characteristics and sun angle differences at different scan angles. The work is ongoing to characterize spatial responses for the M-bands and DNB.

6.4. On-Orbit BBR Characterization

[55] Before launch, the TVac and ambient ground characterization showed that the VIIRS on-orbit BBR was expected to be good [*Lin et al.*, 2011]. In the initial on-orbit Intensive Calibration and Validation campaign, the moon was used for BBR verification of the reflective solar bands that are not saturated by the lunar radiance. The lunar BBR results are satisfactory and are close to the prelaunch measurements as shown in Figure 19.

[56] In the scan direction, VIIRS nests two I-samples into one M-sample in the scan direction (the center of the M-sample is halfway between the centers of the two I-samples). In the track direction, VIIRS nests samples from two I-band detectors into one sample from one M-band detector. VIIRS BBR requirement specifies footprint overlap of band pairs to a certain percentage [*Lin et al.*, 2011]. Detailed verification of VIIRS BBR for the S/MWIR and LWIR bands that are saturated by the moon is ongoing.

7. Discussions

[57] There are several events affecting the VIIRS geometric quality. These include occasional attitude spikes, scan synchronization losses, lunar maneuvers, sector rotations, and star tracker realignments. In addition, recently higher quality digital elevation model (DEM) and land/water masks have been adopted by MODIS and should be used for VIIRS. Finally, the DNB geolocation is currently not available in a terrain corrected form from the NOAA distribution systems such as the Comprehensive Large Array-data Stewardship System.

7.1. RTA and HAM Synchronization Loss

[58] The RTA and HAM synchronization loss was first discovered on 18 November 2011 after 20 days in space. An intensive investigation found that the most likely root cause was that high energy particles in space caused charges to accumulate around the wires in the SCE that resulted in invalid RTA and HAM encoder values. Two types of sync losses were identified: "major" and "minor" lasting about 100 and 10 s each, respectively. When a sync loss occurs, data are misplaced in the scanning cycle and is not usable. The average occurrence of sync loss is about once in 17 days.

[59] As mentioned in section 5, the JPSS Program switched the SCE from side-B to side-A on 22 November 2012. Since then, eight more sync loss events occurred. The last couple of sync losses were on 31 May and 3 June 2013, with a long interval of 129 days from the previous one on 22 January 2013.

7.2. Spacecraft Jitter

[60] High-frequency attitude spikes have been observed in the VIIRS attitude data. The magnitude of these spikes is small (about 10 arc sec peak to peak or ± 40 m at nadir) and only appear about once per orbit for a short time (~2 min). It is not possible to capture the full form of these oscillations because the onboard attitude is only transmitted to the ground once per second. No visible geometric anomalies have been observed during these events, but we plan further analysis to better understand any impact on the VIIRS geometry.

7.3. The Use of Two-Line Elements Backup Data

[61] Because of delivery delays of the spacecraft telemetry, the geolocation algorithm must occasionally use backup orbit data, called two-line elements (TLEs), and nominal spacecraft attitude (geodetic pointing). If these telemetry gaps are less than 16 scans, the geolocation software interpolates the spacecraft position and velocity using quadratic interpolation. For longer gaps, the software switches to the backup TLEs, which can be much less accurate than the onboard orbit data (up to 1 km error). These gaps are rare, but when they do occur, the geolocation accuracy is compromised. When this backup orbit data is used, the scan(s) are identified using a scan level quality flag.

[62] Because of a flaw in the geolocation software, the use of the TLEs may cause an error as large as 20 km. A fix for this was made in the NOAA data system starting 10 July 2013. We plan to continue to work with the JPSS ground system to minimize the use of the TLEs and the impact on the geolocation accuracy when they are used.

7.4. Missing Data When Commanding

[63] Spacecraft maneuvers occur about once per month. These are primarily roll maneuvers for lunar calibration (~monthly) but also include less frequent drag makeup (~1–2 per year), inclination (~every 2 years), pitch, and yaw maneuvers (~once or twice per mission lifetime). During the maneuver and for a period of time after the maneuvers (~1 orbit or ~100 min), the geolocation will not be as accurate because a coarse pointing is used during the maneuvers and a period of time after the maneuvers is needed to return to accurate pointing knowledge. A maneuver flag is set in the geolocation product, but this may not cover the entire time period when the pointing knowledge is low.

[64] Sector rotations are performed for lunar calibration. A sector rotation occurs when the instrument operators command the normally nadir portion of the scan to point to a different location (e.g., the moon) so that the lunar data can be acquired in a portion of the scan with the bands aligned and without bow-tie deletion. These rotations normally happen during lunar maneuvers and so are mostly masked by the maneuvers. However, about once a year, the sector rotations may happen without a maneuver because the moon is visible in the VIIRS space-view port without rolling the spacecraft. We are working to clearly mark these sector rotations so that data during the events are not used in downstream production so that users are aware when they occur.

7.5. Star Tracker Realignments

[65] Based on analysis of star location residuals in the onboard attitude control system, the SNPP flight operations team makes occasional adjustments to the alignment matrices of the two spacecraft star trackers. A small adjustment to one of the star trackers was performed on 25 April 2013, the first since VIIRS began collecting data systematically. Although the adjustment was small (~5 arc sec), the mean of the ground control point residuals after the adjustment clearly showed a ~20 m at nadir change in pointing. Subsequently, an updated geolocation LUT was put into operations to compensate for this change on 23 August 2013. In the future, the flight operations team and the VIIRS geolocation team will work together more closely to ensure that any future star tracker and VIIRS geolocation LUT updates are better coordinated to minimize the time between alignment changes and the LUT updates.

7.6. Ongoing Improvements

[66] The MODIS Science Team recently adopted a higher quality DEM and land/water mask [10, 11] that are being used in the latest Collection 6 (C6) reprocessing. We have advocated that these ancillary data products be used in the production of the operational VIIRS data products.

[67] The current operational VIIRS production system produces ellipsoid and terrain corrected geolocation for the M- and I-bands, but only produces ellipsoid geolocation for the DNB. Since one of the primary applications of the DNB is to study urban areas at night, terrain corrected DNB geolocation is needed to enable users to easily locate high-elevation city lights (e.g., Denver) from off-nadir viewing angles. We are working with NOAA to implement the same terrain correction algorithm for the DNB that is currently used for the other bands in their data system.

8. Summary and Conclusions

[68] The postlaunch analysis of the VIIRS geometric performance is well underway. Overall, the geometric performance in spatial responses, BBR, and geolocation accuracy and precision are very good. Work is ongoing to complete on-orbit measurements of the BBR for the S/MWIR and LWIR bands that are saturated by the moon. Also, the LSF measurements using ground targets are difficult and so the results are preliminary but do not disagree with the prelaunch measurements. We have started working on another method of computing the instrument LSF that uses lunar calibration images. The geolocation accuracy and precision are comparable with those of MODIS [*Wolfe et al.*, 2012] and will be further refined and monitored using our global set of ground control points to account for any seasonal variation and long-term trends in VIIRS' geometric parameters. Overall, the VIIRS' on-orbit geometric performance is good and matches the prelaunch performance and so is expected to meet the needs of both the long-term monitoring and operational communities.

References

Buskila, K., S. Towito, E. Shmuel, R. Levi, N. Kopeika, K. Krapels, R. G. Driggers, R. H. Vollmerhausen, and C. E. Halford (2004), Atmospheric modulation transfer function in the infrared, *Appl. Opt.*, *43*(2), 471–482.

Cao, C., F. DeLuccia, X. Xiong, R. Wolfe, and F. Weng (2013), Early on-orbit performance of the Visible Infrared Imaging Radiometer Suite (VIIRS) onboard the Suomi National Polar-orbiting Partnership (S-NPP) satellite, *IEEE Trans. Geosci. Remote Sens.*, doi:10.1109/TGRS.2013.2247768.

Fang, D. T., and J. Puschell (2010), Imagery spatial performance throughput correction methodology, *Remote Sens. Syst. Eng. III Proc. of SPIE*, *7813*, 15, doi:10.1117/12.860740.

Lee, T. F., S. D. Miller, F. J. Turk, C. Schueler, R. Julian, C. Elvidge, S. Deyo, P. N. Dills, and S. Wang (2004), The day/night visible sensor aboard NPOESS VIIRS, 13th Conference on Satellite Meteorology and Oceanography, Norfolk, VA, 19-23 September 2004.

Lin, G., R. E. Wolfe, and M. Nishihama (2011), NPP VIIRS geometric performance status, in *Earth Observing Systems XVI*, *Proc. of SPIE*, vol. 8153, edited by J. J. Butler, X. Xiaoxiong, and X. Gu, pp. 81531V–81531V-14, San Diego, CA, doi:10.1117/12.894652.

Miller, S. D., S. P. Mills, C. D. Elvidge, D. T. Lindsey, T. F. Lee, and J. D. Hawkins (2012), Suomi satellite brings to light a unique frontier of nighttime environmental sensing capabilities, *Proc. Natl. Acad. Sci. U. S. A.*, *109*(39), doi:10.1073/pnas.1207034109/-/DCSupplemental.

NASA Joint Polar Satellite System (JPSS) (2011), VIIRS Radiometric Calibration Algorithm Theoretical Basis Document (ATBD), document No. 474-00027, Goddard Space Flight Center, Greenbelt, Maryland.

NASA Joint Polar Satellite System (JPSS) Ground Project (2011), Joint Polar Satellite System (JPPS) VIIRS Geolocation Algorithm Theoretical Basis Document (ATBD), document No. 474-00053, Goddard Space Flight Center, Greenbelt, Maryland.

Nishihama, M., R. E. Wolfe, D. Solomon, F. S. Patt, J. Blanchette, A. J. Fleig, and E. Masuoka (1997), MODIS Level 1A Earth Location Algorithm Theoretical Basis Document Version 3.0, SDST-092, Lab. Terrestrial Phys., NASA Goddard Space Flight Center, Greenbelt, MD.

Storey, J., P. Scaramuzza, G. Schmidt, and J. Barsi (2005), "Landsat 7 scan line corrector-off gap-filled product development," in Proceedings of Pecora 16, Global Priorities in Land Remote Sensing, October 23-27, 2005, Sioux Falls, South Dakota.

Wolfe, R. E., and M. Nishihama (2009), Trends in MODIS geolocation error analysis, in *Earth Observing Systems XIV*, *Proc. of SPIE*, vol. 7452, edited by J. J. Butler, X. Xiaoxiong, and G. Xingfa, pp. 74520L, San Diego, CA, doi:10.1117/12.826598.

Wolfe, R. E., M. Nishihama, A. J. Fleig, J. A. Kuyper, D. P. Roy, J. C. Storey, and F. S. Patt (2002), Achieving sub-pixel geolocation accuracy in support of MODIS land science, *Remote Sens. Environ.*, *83*(1-2), 31–49.

Wolfe, R. E., M. Nishihama and J. R. Kuyper (2006), Improving satellite moderate resolution instrument geolocation accuracy in rough terrain, IGARSS: IEEE International Geosci. and Remote Sens. Symposium, 1123-1125.

Wolfe, R. E., M. Nishihama, G. Lin, K. P. Tewari, and E. Montano (2012), MODIS and VIIRS geometric performance comparison, IEEE International Geosci. and Remote Sens. Symposium, Munich, Germany, July, 2012.

Xiong, X., N. Che, and W. Barnes (2005), Terra MODIS on-orbit spatial characterization and performance, *IEEE Trans. Geosci. Remote Sens.*, *43*, 355–365.

Xiong, X., N. Che, W. Barnes, Y. Xie, L. Want, and J. Wu (2006), Status of Aqua MODIS spatial characterization and performance, *Proc. of SPIE*, *6361*, U211–U219, doi:10.1117/12.687162.

Xiong, X., et al. (2013), VIIRS on-orbit calibration methodology and performance, *J. Geophys. Res. Atmos.*, doi:10.1002/2013JD020423, in press.